

Long-term relaxation of one-dimensional self-gravitating systemsMathieu Roule ^{1,*}, Jean-Baptiste Fouvry ¹, Christophe Pichon ^{1,2} and Pierre-Henri Chavanis ³¹*Institut d'Astrophysique de Paris, UMR 7095, 98 bis Boulevard Arago, F-75014 Paris, France*²*IPhT, DRF-INP, UMR 3680, CEA, L'Orme des Merisiers, Bât 774, 91191 Gif-sur-Yvette, France*³*Laboratoire de Physique Théorique, Université de Toulouse, CNRS, UPS, France*

(Received 6 April 2022; accepted 16 August 2022; published 13 October 2022)

We investigate the long-term relaxation of one-dimensional (1D) self-gravitating systems, using both kinetic theory and N -body simulations. We consider thermal and Plummer equilibria, with and without collective effects. All combinations are found to be in clear agreement with respect to the Balescu–Lenard and Landau predictions for the diffusion coefficients. Interestingly, collective effects reduce the diffusion by a factor ~ 10 . The predicted flux for Plummer equilibrium matches the measured one, which is a remarkable validation of kinetic theory. We also report on a situation of quasikinetic blocking for the same equilibrium.

DOI: [10.1103/PhysRevE.106.044118](https://doi.org/10.1103/PhysRevE.106.044118)**I. INTRODUCTION**

As a result of violent relaxation [1], a self-gravitating system reaches, in a few dynamical times, a quasistationary state (QSS) where the mean-field dynamics is frozen on a stationary solution of the Vlasov-Poisson equations. Yet, this mean-field state is generically not the system's thermodynamical equilibrium. Even when isolated, QSSs slowly evolve under the effects of perturbations through Poisson shot noise, i.e., the slight difference between the smooth mean-field distribution and the discrete one realised from a finite number of particles. Linear response theory describes the short-term evolution of these fluctuations, driven both by the mean-field potential and the self-induced potential fluctuations. This last contribution constitutes a feedback loop, which we refer to as collective effects. These are the gravitational counterpart of Debye shielding in plasma physics. Its analysis gives valuable insights on the system's linear stability [2]. On longer timescales, these time-correlated fluctuations govern the reshuffling of the system's mean-field distribution of orbits, hence driving the system toward different QSSs. This long-term evolution ultimately ends at thermodynamical equilibrium described by the Boltzmann distribution, when such maximal entropy states exist.

The master equation describing the nonlinear long-term evolution of isolated discrete self-gravitating systems is the so-called inhomogeneous Balescu–Lenard (BL) equation [3,4]. While particularly valuable, this kinetic framework derived a decade ago relies on specific sets of asymptotic assumptions, e.g., small perturbations, associated kinetic truncations, timescale separation between fluctuations and mean-field evolution, which may not be strictly fulfilled in practice. Quantitative validation is therefore of interest. Such assessments have been attempted both for razor thin discs and spherical isotropic clusters [see, e.g., [5,6]]. However, the

large dimension of phase space in these 2D and 3D systems made comparisons to the corresponding N -body simulations challenging. These works offered some qualitative agreement between the kinetic predictions and simulations. Yet, the quantitative accuracy of the match remained limited, in particular because predictions require repeated costly integrals over phase space, while preserving long-term numerical precision in the simulations is challenging.

This is the motivation for the present work, which aims at performing such a thorough comparison for one-dimensional self-gravitating systems, whose reduced phase-space dimension allows for finer precision. Both violent [see, e.g., [7–9]] and long-term [see, e.g., [10–13]] relaxations of 1D self-gravitating systems have extensively been explored through numerical simulations. Here, we predict and analyze the long-term relaxation of such systems in the light of recent theoretical developments in kinetic theory.

Interestingly, such a 1D model corresponds to a proxy for more realistic astrophysical systems, such as the vertical diffusion of stars [see, e.g., [14,15]], or the onset of large scale structure formation in the early universe [see, e.g., [16,17]]. Building upon [18], which considered the long-term evolution of the Hamiltonian mean field (HMF) in its inhomogeneous phase, the present investigation is also interesting in what it shares or not with self-gravitating systems of higher dimension.

Here, we aim at achieving a better understanding of the mechanisms governing the long-term evolution of discrete self-gravitating systems, while accounting for collective effects (BL) or neglecting them (Landau). This double analysis provides key informations on the influence of collective effects on a system's evolution. The paper is organized as follows. Section II presents the model and the explored quasiequilibria. Section III computes their long-term resonant relaxation. Section IV explains the role of collective effects and profile shapes in the system's long-term evolution, while

*roule@iap.fr

Sec. V sums up the lessons learned from this study case. All technical details are given in the Appendices.

II. MODELS

A. 1D self-gravitating systems

We consider a population of N particles of individual mass $m = M_{\text{tot}}/N$, with M_{tot} the system's total mass, fixed throughout the paper. Particles are confined to an infinite line and coupled to one another via the specific pairwise interaction potential,

$$U(x, x') = G|x - x'|, \quad (1)$$

with G the gravitational constant, and (x, x') the respective positions of the two interacting particles. As such, the potential generated at position x by a mass m at position x' is $mU(x, x')$. This interaction corresponds to infinite parallel planes of uniform surface mass density attracting one another through the classical 3D Newtonian interaction. The potential, $\psi(x)$, and density, $\rho(x)$, are linked via Poisson's equation,

$$\Delta\psi = 2G\rho, \quad (2)$$

making the force between two particles independent of their separation. The 1D gravitational potential differs from its 3D counterpart in two respects: (i) it is unbounded at large separation, hence all particles are trapped (i.e., no escapers are possible); (ii) it is finite at zero separation allowing particles to cross one another.

Following an initial violent relaxation [1], the system's mean state can be described by its ensemble-averaged distribution function (DF), $F = F(x, v, t)$, with v the velocity, and normalized so that $\int dx dv F = M_{\text{tot}}$. As all 1D equilibria are integrable, such a QSS can most efficiently be described via the angle-action coordinates (θ, J) , with J the action, and θ the associated 2π -periodic angle (see Appendix A1 for details). In the absence of perturbations, the angle evolves linearly in time with the orbital frequency $\Omega(J) = \partial H/\partial J$ where $H = v^2/2 + \psi(x)$ is the specific energy and $\psi(x) = \int dx' dv' F(x', v')U(x, x')$ the system's mean-field potential. In the following, we use equivalently J or the specific (unperturbed) energy E to label orbits.

As a result of potential fluctuations induced by the finite number of particles, this QSS, $F = F(J, t)$, undergoes a slow and irreversible long-term relaxation, captured by the inhomogeneous BL equation [3,4]. Testing this prediction is the focus of this work.

B. Thermodynamic and quasistationary equilibria

We consider two explicit quasistationary distributions: (i) the global thermodynamical equilibrium; and (ii) a more peaked QSS, analog of the 3D Plummer sphere, as we now detail.

Unlike their 3D analogs (unless confined in a box with repulsive walls) [19–21], 1D self-gravitating systems have a well-defined maximum entropy equilibrium state. Under the constraints of fixed total mass and energy, its density follows [10,22–24]

$$\rho(x) = \frac{M_{\text{tot}}}{2\Lambda} \operatorname{sech}^2(x/\Lambda), \quad (3)$$

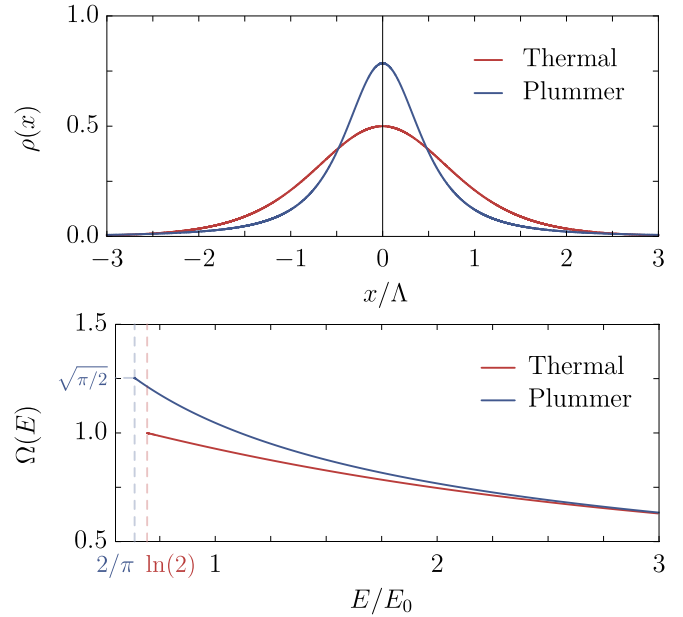


FIG. 1. Top: Density profiles of the thermal and Plummer equilibria. The Plummer equilibrium has a sharper core. Bottom: Corresponding frequency profiles. The range of available frequencies is wider for the Plummer equilibrium.

with Λ the system's characteristic length (see Appendix A6 for the associated potential), while its DF reads

$$F(E) = \frac{2M_{\text{tot}}}{\sqrt{\pi}\sigma\Lambda} \exp(-2E/E_0), \quad (4)$$

with $\sigma = \sqrt{GM_{\text{tot}}\Lambda}$, and $E_0 = GM_{\text{tot}}\Lambda$ the characteristic velocity and specific energy. We emphasize that the DF from Eq. (4) cannot further relax by design. Naturally, this does not prevent individual particles from undergoing themselves a diffusion.

We also investigate an equilibrium stemming from polytropes [25–27]. More precisely, by analogy with the 3D Plummer sphere, we consider the 1D density

$$\rho(x) = \frac{M_{\text{tot}}}{2\alpha} [1 + (x/\alpha)^2]^{-3/2}, \quad (5)$$

where $\alpha = 2\Lambda/\pi$ ensures that this distribution has the same energy as Eq. (3). The associated DF follows the power-law distribution (see Appendix A6),

$$F(E) = \frac{15G^3M_{\text{tot}}^4\alpha^2}{32\sqrt{2}} E^{-7/2}. \quad (6)$$

In Fig. 1, we illustrate the density and frequency profiles of these two states. While the thermodynamical equilibrium has a strong core and few particles in the tails (only $\sim 10^{-9}M_{\text{tot}}$ outside $[-10\Lambda, 10\Lambda]$), the Plummer distribution has a sharper core and much wider tails ($\sim 10^{-3}M_{\text{tot}}$ outside $[-10\Lambda, 10\Lambda]$). In the second panel of Fig. 1, we present the frequency profile of both equilibria. The Plummer denser core widens its frequency profile, allowing in turn for more resonances. At high energies, both frequency profiles decrease like $1/\sqrt{E}$.

III. LONG-TERM EVOLUTION

The long-term relaxation of self-gravitating systems driven by finite- N fluctuations is generically governed by the inhomogeneous BL equation [3,4],

$$\frac{\partial F(J, t)}{\partial t} = -2\pi^2 m \frac{\partial}{\partial J} \left\{ \sum_{k, k'} k \int dJ' |\psi_{kk'}^d[J, J', k \Omega(J)]|^2 \delta_D[k \Omega(J) - k' \Omega(J')] \left(k' \frac{\partial}{\partial J'} - k \frac{\partial}{\partial J} \right) F(J) F(J') \right\}. \quad (7)$$

This nonlinear equation describes the long-term evolution of the mean orbital distribution, $F(J, t)$, driven by resonant couplings between gravitationally dressed Poisson fluctuations ($m \propto 1/N$). The sum, $\sum_{k, k'}$, and integral, $\int dJ'$, in Eq. (7) correspond to a scan over the discrete resonances and orbital space. Any time the resonance condition, $k \Omega(J) - k' \Omega(J') = 0$, is met, the diffusion is sourced. The system's propensity to amplify fluctuations is captured in the dressed susceptibility coefficients, $|\psi_{kk'}^d(J, J', k \Omega)|^2$. Those are the (squared norm of the) Fourier transform (FT) of the pairwise interaction potential dressed by the system's gravitational susceptibility (see Appendix A 3). When neglecting collective effects, these dressed coefficients are replaced by the bare ones $\psi_{kk'}^d(J, J', \omega) \rightarrow \psi_{kk'}(J, J')$ (see Appendix A 4), giving the inhomogeneous Landau equation [28]. In the following, we investigate both cases where the gravitational dressing is (BL) and is not (Landau) taken into account.

A. Orbital diffusion

The BL Eq. (7) can be rewritten as a more compact continuity equation in action space

$$\frac{\partial F}{\partial t} = - \frac{\partial \mathcal{F}}{\partial J} \quad (8a)$$

$$= - \frac{\partial}{\partial J} \left[A(J) F(J) - \frac{1}{2} D(J) \frac{\partial F}{\partial J} \right], \quad (8b)$$

with the total flux $\mathcal{F}(J, t)$, and the diffusion coefficient

$$D(J) = (2\pi)^2 m \sum_{k, k'} k^2 \int dJ' |\psi_{kk'}^d[J, J', k \Omega(J)]|^2 \times \delta_D[k \Omega(J) - k' \Omega(J')] F(J'). \quad (9)$$

In Eq. (8b), the friction by polarization, $A(J)$, is obtained from Eq. (9) via the substitutions $(2\pi)^2 \rightarrow 2\pi^2$, $k^2 \rightarrow k k'$ and $F \rightarrow \partial F / \partial J'$. As discussed in Sec. 7.4.2 of Ref. [2], the diffusion coefficient also has the simple interpretation

$$D(J) = \lim_{T \rightarrow +\infty} \frac{\langle \Delta J^2(T) \rangle}{T}, \quad (10)$$

with $\Delta J(T) = J(t = T) - J(t = 0)$ the change in action of a given particle, and $\langle \cdot \rangle$ the ensemble average over realisations. Equations (9) and (10) provide us with two independent means of measuring and predicting $D(J)$. In the following, we will focus our interest on the diffusion coefficients in energy, which naturally read $D_{EE} = \Omega^2 D$.

The Landau diffusion corresponds to the case where the diffusion is driven by initial Poisson fluctuations that flow along unperturbed mean-field orbits. The associated simulation procedure is presented in Appendix B 1.

B. Diffusion coefficients

In the top panel of Fig. 2, we present the diffusion coefficients at thermal equilibrium computed with the BL and the Landau formalism, together with the corresponding estimates from numerical simulations. We refer to Appendix A for the details of the kinetic estimation, and Appendix B for the N -body measurements. In both Landau and BL cases, we recover a very good match between the kinetic theory and the numerical measurements. This confirms that, indeed, long-range resonant couplings are responsible for the long-term relaxation of these systems. We stress that the BL diffusion coefficients are ~ 10 times smaller than the Landau ones, an effect already noted in the HMF model for highly magnetized thermal equilibria [see Fig. 9 in [18]]. This is at variance with the low magnetization HMF result, or the case

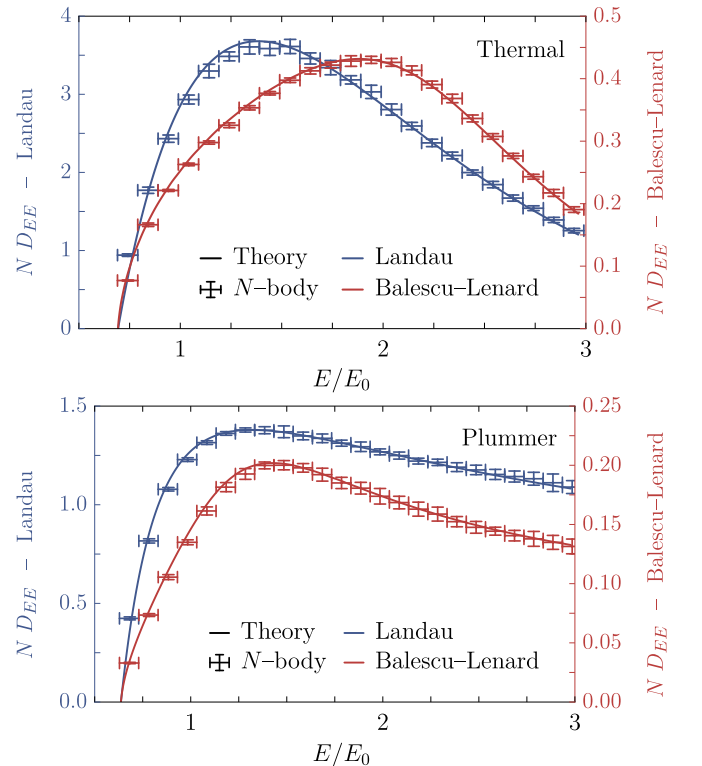


FIG. 2. Top: Diffusion coefficients at thermal equilibrium as a function of energy in both Landau (i.e., without collective effects) and BL (i.e., with collective effects) cases. Bottom: Same as the top panel but for the Plummer equilibrium. The kinetic theory shows a very satisfactory match to the numerical measurements. Note that both measurements have their own vertical scales as collective effects slow down diffusion by a factor ~ 10 . See Appendix B 2 for the numerical details.

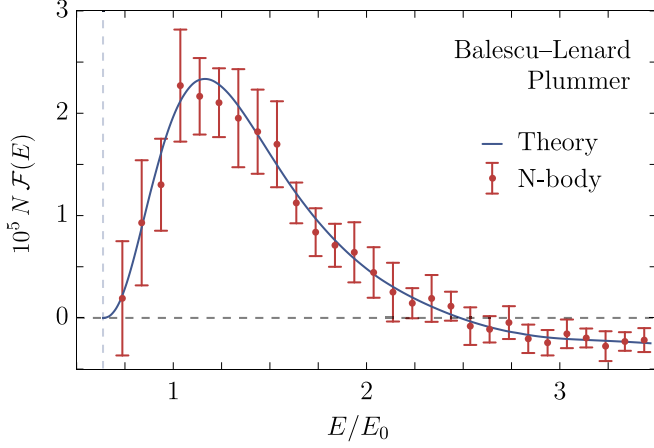


FIG. 3. Initial flux in the Plummer equilibrium as a function of energy predicted by kinetic theory (line) and measured in N -body simulations (points). Both capture the maximum near $E/E_0 \simeq 1.25$, and the change of sign at $E/E_0 \simeq 2.5$. We stress that the amplitude of $N\mathcal{F}(E)$ has been rescaled by 10^5 . See Appendix B 3 for the numerical details.

of self-gravitating stellar disks [5] where collective effects considerably accelerate the relaxation.

In the bottom panel of Fig. 2, we present the same measurements for the Plummer distribution. Satisfactorily, this other equilibrium shows the same level of fine agreement. Similarly, we also find that collective effects slow down the diffusion by a factor ~ 10 . This will be discussed in Sec. IV.

C. Fluxes

We now turn our interest to the initial diffusion flux, $\mathcal{F}(J, t = 0)$, as given by Eq. (8). Of course, this flux vanishes for the thermodynamical equilibrium. In Fig. 3, we illustrate the initial diffusion flux for a fully self-gravitating Plummer equilibrium. Once again, the kinetic theory and numerical simulations are found to be in a good agreement, and both recover the (slow) relaxation of the Plummer distribution toward the thermal one. Using appropriate dimensionless units, the diffusion flux is typically $\sim 10^5$ times smaller than the diffusion coefficients, i.e., the efficiency of the relaxation is drastically hampered by a partial “kinetic blocking.” This is further discussed in Sec. IV A.

D. Correlation of the perturbations

Following Ref. [29], we present in Fig. 4 the correlation $C(t)$ of the potential fluctuations in the N -body simulations, as a function t/t_{dyn} , with $t_{\text{dyn}} = \Lambda/\sigma$, the dynamical time. This correlation sources orbital diffusion [30]. We refer to Appendix B 4 for a precise definition of $C(t)$. The gravitational dressing has two main effects: (i) it weakens the overall amplitude of the potential fluctuations; (ii) it reduces the coherence time of these perturbations. Indeed, while the Landau correlations decrease like $1/t^2$, the BL correlations are found to decay like $1/t^5$ (see Fig. 12 in Appendix B 4). Naturally, this drives a slower orbital diffusion in the BL situation compared to the Landau one, as presented in Sec. III A.

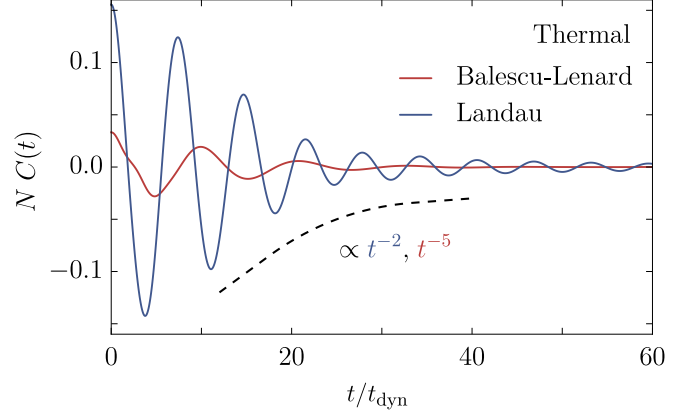


FIG. 4. Time correlation, $C(t)$, of the potential fluctuations in N -body simulations for the thermal equilibrium with and without collective effects. See Appendix B 4 for precise definitions. In the presence of collective effects, both the amplitude and coherence time of the correlation function are reduced.

This is fully consistent with Fig. 5 where we equivalently illustrate the diffusion of individual test particles in the presence/absence of collective effects. In that figure, we also recover that the energy diffusion is naturally modulated at the frequency $\sim 2\pi/t_{\text{dyn}}$, i.e., the typical frequency of the background thermal equilibrium.

IV. DISCUSSION

We now discuss our two main findings: nonthermal equilibria present very inefficient relaxation; and collective effects reduce the efficiency of diffusion.

A. Quasi kinetic blocking

In Fig. 3, we noted that, within appropriate dimensionless units, the diffusion flux in the Plummer equilibrium is $\sim 10^5$

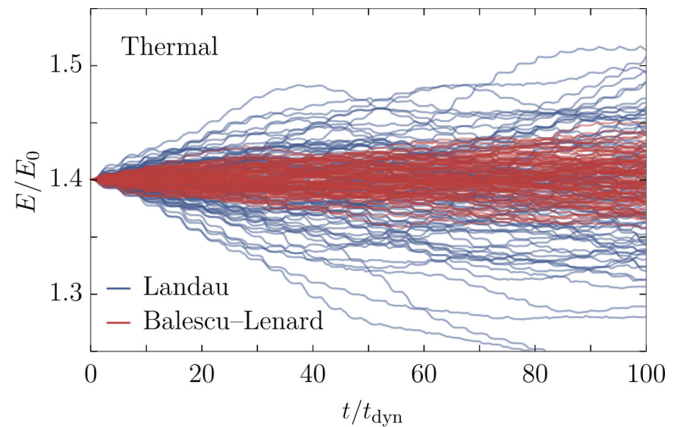


FIG. 5. Typical diffusion of test particles embedded within N -body realizations of the thermal equilibrium with collective effects (BL) or without (Landau). The massless test particles are all placed at the same initial phase-space location in their respective realizations. Collective effects slow down the orbital diffusion.

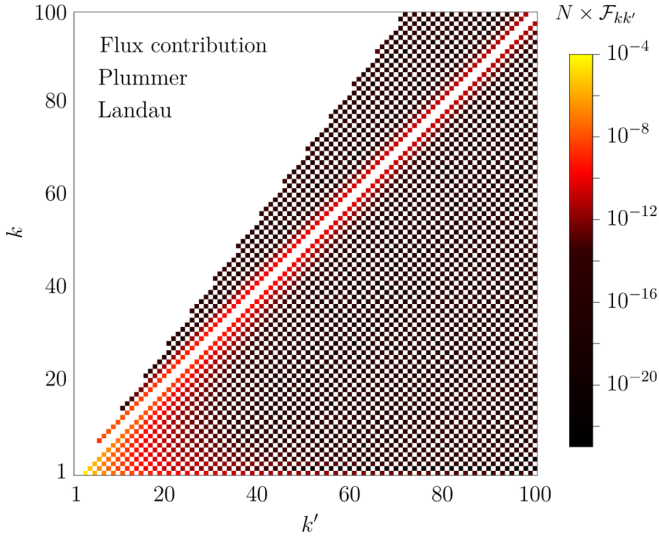


FIG. 6. Individual contributions of the various resonances (k, k') to the initial Landau flux, $\mathcal{F}(E, t = 0)$, for the Plummer equilibrium at $E = \psi(2\alpha)$. By symmetry, we only consider $k, k' \geq 0$ resonances. Note the logarithmic color coding. The flux is dominated by low order resonances and suffers from many annihilating conspiracies (see main text).

times smaller than the associated diffusion coefficients (see Fig. 2). This is the imprint of a quasikinetic blocking, highlighting the system's difficulty to populate resonances driving an efficient diffusion.

As put forward in Eq. (7), the system's long-term diffusion is sourced by resonant interactions. For a given resonant pair (k, k') , one has to ensure that the resonance condition, $k\Omega(J) - k'\Omega(J') = 0$, is met, while the overall efficiency of this coupling is governed by the susceptibility coefficients, $\psi_{kk'}^d(J, J', \omega)$, for that pair. In practice, a couple of important “conspiracies,” responsible for the small flux observed in Fig. 3, operate:

(1) The Plummer frequency profile is monotonic (see Fig. 1). Any resonance $k = k'$ systematically imposes $J = J'$, leading to an exactly vanishing flux in Eq. (7).

(2) Symmetry imposes $\psi_{kk'}^d = 0$, for all k, k' of different parity (see Appendix A 4). As a consequence, one must have $|k - k'| \geq 2$ for a resonance to contribute to the flux. Similarly, k, k' must also have the same sign.

(3) Despite its denser core, the overall frequency range of the Plummer profile is still finite (see Fig. 1). For a given orbit J , this imposes $k/k' \leq \Omega(J = 0)/\Omega(J)$ for the resonance condition from Eq. (7) to be met.

(4) For k large enough, the bare susceptibility coefficients asymptotically scale like $\psi_{kk}(J, J) \propto 1/k^2$ (see Appendix A 4). The higher order the resonance, the less efficient the coupling, and hence the (drastically) smaller the contribution to the flux.

We highlight these different effects in Fig. 6, where we isolate the contributions, $\mathcal{F}_{kk'}$, of the different resonances (k, k') to the Landau flux $\mathcal{F} = \sum_{k, k' > 0} \mathcal{F}_{kk'}$. We emphasize in particular the rapid decay of the flux contributions as k, k' increase and as one moves away from the diagonal $k = k'$ (which only contributes to the diffusion coefficient and not

the flux). These different effects are jointly responsible for the small flux reported in Fig. 3.

Figure 6 is essentially left unchanged when taking into account collective effects. The only significant difference in the BL case is the reduced contribution from the resonances with $k = 1$ for which gravitational dressing weakens the amplitude of the orbital coupling as detailed in Secs. IV B and IV C. Taking collective effects into account therefore further reduces the flux as they notably damp contributions from the resonance $(k, k') = (1, 3)$, the main contributor to the Landau flux (see Fig. 6).

Despite this relative inefficiency, we stress that the Plummer equilibrium still relaxes through $1/N$ two-body resonant effects. This is in stark contrast with homogeneous 1D systems which are generically kinetically blocked at order $1/N$ [see, e.g., [4]] and require the derivation of appropriate kinetic equations at order $1/N^2$ sourced by three-body effects [31].

B. Linear response

We now discuss the influence of collective effects. The efficiency of the gravitational dressing of perturbations is generically captured by the response matrix, $\mathbf{M}(\omega)$ [see, e.g., Eq. (5.94) in [2]] which reads here

$$\mathbf{M}_{pq}(\omega) = 2\pi \sum_{k \in \mathbb{Z}} \int dJ \frac{k \partial F / \partial J}{\omega - k \Omega(J)} \psi_k^{(p)*}(J) \psi_k^{(q)}(J), \quad (11)$$

with $\psi_k^{(p)}(J)$ the FT of the biorthogonal basis elements. As detailed in Appendix A 2, we construct natural basis elements by periodizing the interaction potential on a *ad hoc* length L . This choice impacts the system only on large separations (i.e., small frequencies), which we alleviate by picking L sufficiently large given the system's density. We refer to Appendix A 5 for details on the computation of the response matrix, in particular regarding the resonant denominator from Eq. (11).

In Fig. 7, we illustrate the determinant of the susceptibility matrix $[\mathbf{I} - \mathbf{M}(\omega)]^{-1}$ for the thermal equilibrium, as a function of ω/Ω_0 , with $\Omega_0 = \sqrt{GM_{\text{tot}}/\Lambda}$ the (maximum) orbital frequency in the system's center ($\Omega_0 = \sqrt{GM_{\text{tot}}/\alpha}$ for the Plummer equilibrium). Because the system possesses a finite maximum frequency, Ω_0 , its linear response shows clear signatures at every (resonant) multiple of this frequency. Nonetheless, we find that the collective amplification remains limited, while the same result also holds for the Plummer equilibrium. Conversely, collective effects significantly damp the contribution of the odd resonances $k\Omega \sim \Omega_0$, i.e., the lowest order resonances in the most populated regions. These resonances being dominant contributors to the diffusion (see Sec. IV C), it explains the relative inefficiency of the BL diffusion unveiled in Fig. 2.

C. Impact of collective effects

The influence of the gravitational dressing strongly depends on the resonance frequency, $\omega = k\Omega$. It is therefore of interest to pinpoint the individual contributions of resonances to the diffusion coefficient, $D = \sum_{k, k' > 0} D_{kk'}$.

As for the flux, the allowed resonances must satisfy a parity criterion as well as $k/k' \leq \Omega(J = 0)/\Omega(J)$, but, however,

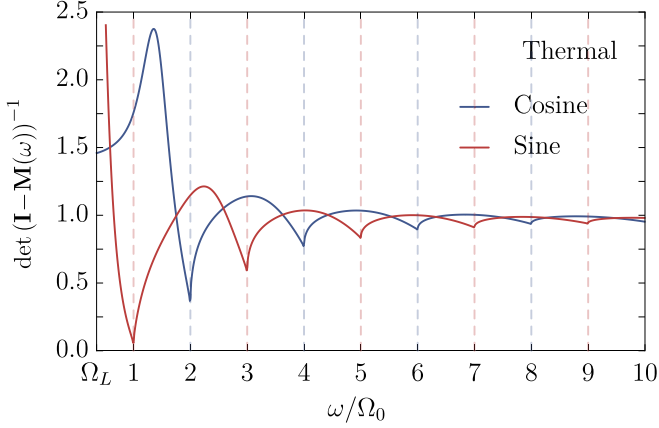


FIG. 7. Determinant of the susceptibility matrix, $[\mathbf{I} - \mathbf{M}(\omega)]^{-1}$, as a function of the real frequency ω/Ω_0 for the even (cosine) and odd (sine) basis elements (see Appendix A 2). Here, Ω_0 is the maximum frequency in the system's center, while $\Omega_L \simeq 0.35 \Omega_0$ is the smallest frequency captured by the L -periodized potential ($L = 10 \Lambda$). Collective effects become negligible at small separation (high frequencies). Conversely, they induce a striking damping for frequencies $\omega \sim \Omega_0$, which explains the particular inefficiency of the BL diffusion compared to the Landau one.

$k = k'$ resonances contribute to the diffusion. Given that the coupling efficiency rapidly drops with the order of the resonance, in Fig. 8, we focus on the contributions of low-order resonances. The top panel of this figure illustrates the predominant role of the resonance $(k, k') = (1, 1)$ in the Landau orbital diffusion (in yellow), while the bottom panel shows the extinguishing role of collective effects for any $k = 1$ resonances. This is ultimately responsible for the relative inefficiency of the BL diffusion w.r.t. the Landau one. The determinant of the susceptibility matrix plotted in Fig. 7 allows us to reach the same conclusions. Indeed, the gravitational susceptibility suffers from a drought for any odd resonant couplings with $\omega \sim \Omega_0$. And, the slight amplification of the resonance $(2, 2)$ observed in Fig. 8 is equivalently found in Fig. 7 since $2\Omega(2\alpha) \sim 1.4\Omega_0$. This amplification still remains too limited to compensate for the strong collective damping of the dominating $(1, 1)$ resonance.

V. CONCLUSIONS

The long-term relaxation of discrete self-gravitating systems is driven by the subtle combined effects of finite- N Poisson fluctuations and long-range orbital resonances, possibly boosted or damped by gravitational polarization. This diffusion of the orbital structure is captured by the inhomogeneous BL equation [3,4]. In this work, we compared its kinetic predictions with N -body simulations of 1D self-gravitating systems.

We focused on the thermal and Plummer equilibria, while accounting and not accounting for collective effects. We reach clear agreement for both models on the rate of diffusion. The BL diffusion coefficients were found to be ~ 10 times smaller than the Landau ones, i.e., collective effects surprisingly mitigate diffusion, and we provided an explanation for it. This conclusion is particularly interesting as it is also present in the

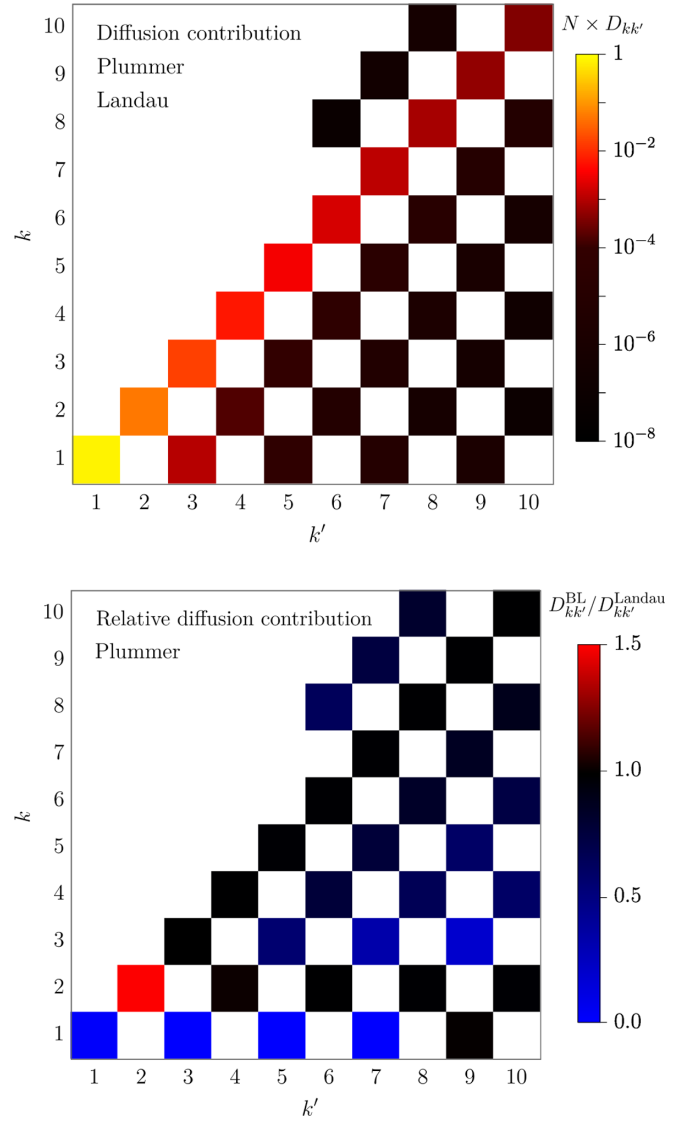


FIG. 8. Top: Individual contributions of the various resonances (k, k') to the Landau diffusion coefficients for the Plummer equilibrium and $E = \psi(2\alpha)$. Bottom: Relative contributions when collective are or not taken into account, for the same setup. The main contributor to the Landau diffusion, resonance $(1, 1)$, is severely damped by collective effects, while the amplification of other resonances remains limited.

HMF model in highly magnetized equilibria [18] while it is absent in weakly magnetized ones or in the periodic stellar cube [32]. This may or may not be the case in higher dimensions [see, e.g., [5,6,33]] possibly depending on the position and geometry of the wake and on these systems' reservoirs of free energy via rotation or anisotropy.

Similarly, the predicted flux closely matches the measured one for the Plummer equilibrium. This is a remarkable validation of kinetic theory, which was not granted *a priori*, since the BL theory makes strong assumptions about the amplitude of the fluctuations and timescale decoupling between the linear and long-term processes. We discussed how diffusion is mostly driven by low order resonances which can be significantly altered by collective effects. We explained

how the vanishing contribution of $k = k'$ resonances to the flux leads to a quasikinetic blocking, drastically slowing down the relaxation of nonthermal equilibria.

Beyond this work, one should aim at better understanding the precise origin of the ability of collective effects to accelerate/slow down relaxation. For example, one could investigate sets of equilibria closer to marginal stability, e.g., with bumps on tail, and identify the possible importance of their damped modes [see, e.g., [34]]. In the spirit of the low magnetization HMF model [18], one may expect that collective modes would ultimately boost the BL flux over the Landau one.

Given the accuracy achieved for the initial flux, it would clearly be useful to integrate Eq. (7) self-consistently in time. This is no easy undertaking, as it involves tracking both the nonlinear dependence in F and the joint evolution of the mean potential and the associated angle-action coordinates [see, e.g., [35]]. This same 1D model may also prove useful to understand the relaxation of thickened galaxies [see, e.g., [36]]. More generally, it bodes well for future implementations in higher dimensions, as in globular clusters, or dark matter halos.

ACKNOWLEDGMENTS

This work is partially supported by the Agence Nationale de la Recherche (Grant Segal ANR-19-CE31-0017 [37]) and by the IDEX Sorbonne Université. We thank S. Rouberol for the smooth running of the Infinity cluster, where the simulations were performed. We thank K. Tep and M. Petersen for many stimulating discussions. The codes underlying the present work are available online [38].

APPENDIX A: 1D KINETIC THEORY

1. Angle-action coordinates

Following Eq. (3.195) of Ref. [2], the action of an orbit is the circulation of v for one full radial oscillation. For an even mean-field potential $\psi(r = |x|)$, it simply reads

$$J = \frac{1}{\pi} \int_{-r_a}^{r_a} dx v = \frac{2\sqrt{2}}{\pi} \int_0^{r_a} dr \sqrt{\psi(r_a) - \psi(r)}, \quad (\text{A1})$$

with r_a the orbit's apocenter, i.e., the maximum radius reached during the particle's libration which satisfies $E = \psi(r_a)$. In the following sections, we equivalently use r_a , E , and J to label orbits. The orbital frequency, $\Omega = \partial H / \partial J$, and the associated angle θ , satisfying $\dot{\theta} = \Omega$, read

$$\frac{1}{\Omega} = \frac{\sqrt{2}}{\pi} \int_0^{r_a} \frac{dx}{\sqrt{\psi(r_a) - \psi(x)}}, \quad (\text{A2a})$$

$$\theta(x, r_a) = \frac{\Omega(r_a)}{\sqrt{2}} \int_{\mathcal{C}} \frac{dx'}{\sqrt{\psi(r_a) - \psi(x')}}, \quad (\text{A2b})$$

with \mathcal{C} the contour going from $x = -r_a$ up to the current position $x = x(\theta)$ along the radial oscillation. Therefore, the angle mapping is such that

$$x(\theta = 0) = -r_a, \quad x\left(\frac{\pi}{2}\right) = 0, \quad x(\pi) = r_a, \quad x\left(\frac{3\pi}{2}\right) = 0. \quad (\text{A3})$$

To cure the divergence of the integrand of Eq. (A2) for $x \rightarrow \pm r_a$, we perform the change of variables $x = r_a f(u)$ toward an effective anomaly $-1 \leq u \leq 1$ satisfying $f(\pm 1) = \pm 1$ and $f'(\pm 1) = 0$. This change of variable must be: (i) explicit (no inversion needed), (ii) stable (to sample numerous nearby points), (iii) generic (must work for any analytic potential). In practice, we use the polynomial anomaly $f(u) = u\left(\frac{3}{2} - \frac{1}{2}u^2\right)$ [39].

To address the arising 0/0 limit in the integrand

$$I(u, r_a) = \frac{r_a f'(u)}{\sqrt{\psi(r_a) - \psi[r_a f(u)]}}, \quad (\text{A4})$$

we use a second-order Taylor expansion in $u \rightarrow \pm 1$ and $r_a/\Lambda \rightarrow 0^+$, as soon as $|1 \pm u| \leq 10^{-3}$ or $r_a/\Lambda \leq 10^{-3}$. Benefiting from this numerically stable approach, the integrals from Eqs. (A1) and (A2) are computed using Simpson's 1/3-rule, with 100 uniform intervals in $u \in [0, 1]$.

2. Biorthogonal basis

Following Ref. [40], the biorthogonal basis elements satisfy

$$\psi^{(p)}(x) = \int dx' \rho^{(p)}(x') U(x, x'), \quad (\text{A5a})$$

$$\int dx \rho^{(p)}(x) \psi^{(q)*}(x) = -\delta_{pq}. \quad (\text{A5b})$$

With them, the pairwise interaction potential becomes

$$U(x, x') = - \sum_p \psi^{(p)}(x) \psi^{(p)*}(x'). \quad (\text{A6})$$

To construct basis elements, we periodize $U(x, x')$ on a period $2L$, so that it becomes $U_{\text{per}}(x, x') = U(x, x')$ for $|x - x'| \leq L$, and $U_{\text{per}}(x + 2kL, x') = U_{\text{per}}(x, x')$ for $k \in \mathbb{Z}$. Dropping the constant term, the periodized potential, U_{per} , is decomposed in Fourier series via

$$U_{\text{per}}(x, x') = - \frac{4GL}{\pi^2} \sum_{\substack{p \text{ odd} \\ p > 0}} \frac{1}{p^2} \left[\cos\left(p \frac{\pi}{L} x\right) \cos\left(p \frac{\pi}{L} x'\right) + \sin\left(p \frac{\pi}{L} x\right) \sin\left(p \frac{\pi}{L} x'\right) \right]. \quad (\text{A7})$$

Following Eq. (A6), the natural basis elements are then

$$\psi_{\text{even}}^{(p)}(x) = \frac{2\sqrt{GL}}{p\pi} \cos\left[p \frac{\pi}{L} x\right], \quad (\text{A8})$$

with $p > 0$ odd, and their odd counterpart $\psi_{\text{odd}}^{(p)}$ via $\cos \rightarrow \sin$. Following Eq. (2), the associated densities are

$$\rho_{\text{even}}^{(p)}(x) = \frac{-\pi^2 p^2}{2GL^2} \psi_{\text{even}}^{(p)}(x), \quad (\text{A9})$$

and equivalently for the odd ones. It is straightforward to check that Eqs. (A8) and (A9) comply with Eq. (A5) for the periodized potential, U_{per} , when restricting the integration range to $-L \leq x \leq L$.

In practice, the basis elements are computed from coupled recurrence relations [see Eq. (5.4.6) in [41]]. In the main text, we use a periodization length $L = 10\Lambda$ (respectively, $L = 100\Lambda$) and 256 (respectively, 1024) basis elements for

thermal (respectively, Plummer) computations. Indeed, since the Plummer equilibrium density has wide tails (see Fig. 1), a large L is required which, in turn, requires more basis elements to reach a sufficient resolution.

3. Fourier transform in angles

Once a suitable biorthogonal basis has been constructed, one has to compute the FT of the basis element, $\psi_k^{(p)}(J)$, involved in both the response matrix from Eq. (11) and the dressed coupling coefficient

$$\psi_{kk'}^d(J, J', \omega) = - \sum_{p,q} \psi_k^{(p)}(J) [\mathbf{I} - \mathbf{M}(\omega)]_{pq}^{-1}(\omega) \psi_{k'}^{(q)*}(J'), \quad (\text{A10})$$

with \mathbf{I} the identity matrix, and $\mathbf{M}(\omega)$ the system's response matrix defined in Eq. (11). Given the convention from Eq. (A3), the FT of the basis elements reads

$$\psi_k^{(p)}(J) = \frac{1}{\pi} \int_0^\pi d\theta \psi^{(p)}(x[\theta, J]) \cos(k\theta). \quad (\text{A11})$$

To compute this integral, we naturally perform the same change of variables as in Appendix A1. One is left with two integrals that must be performed simultaneously

$$\psi_k^{(p)}(J) = \frac{1}{\pi} \int_{-1}^1 du \frac{d\theta}{du} \psi^{(p)}(x[u]) \cos(k\theta[u]), \quad (\text{A12a})$$

$$\theta[u] = \int_{-1}^u du' \frac{d\theta}{du'}, \quad (\text{A12b})$$

where $d\theta/du = \Omega(r_a)I(u, r_a)/\sqrt{2}$ with $I(u, r_a)$ defined in Eq. (A4). Although the integrals from Eqs. (A12) seem nested, they can be evaluated via the single integral of a 2-vector [42]. In practice, we use a fourth-order Runge-Kutta (RK4) scheme with 10^3 steps for $u \in [-1, 1]$.

4. Bare coupling coefficients

In the Landau case, collective effects can be neglected. As such, in Eq. (A10), one makes the replacement $[\mathbf{I} - \mathbf{M}(\omega)]^{-1} \rightarrow \mathbf{I}$, and the dressed coupling coefficients, $\psi_{kk'}^d(J, J', \omega)$ become the bare ones, $\psi_{kk'}(J, J')$. Importantly, these coefficients can be computed without any basis expansion, as they are the Fourier transform of the pairwise interaction w.r.t. the angle θ [28]. Using the effective anomaly u from Appendix A1, the frequency-independent bare coupling coefficients become

$$\psi_{kk'}(J, J') = \frac{1}{\pi^2} \int_{-1}^1 du du' g(x) g'(x') U(x, x'), \quad (\text{A13})$$

with $g(x) = \cos(k\theta) d\theta/du$ (and similarly for g'). Symmetry imposes $\psi_{kk'}(J, J') = 0$ for any k, k' of different parity. The same result also holds for the dressed susceptibility coefficients, $\psi_{kk'}^d(J, J', \omega)$, from Eq. (A10).

To compute Eq. (A13), each anomaly, u, u' , is sampled with K nodes at the location $u_i = -1 + 2(i - \frac{1}{2})/K$ with $1 \leq i \leq K$. Equation (A13) becomes

$$\psi_{kk'}(J, J') = \frac{4G}{\pi^2 K^2} \sum_{i,j=1}^K g_i g'_j |x_i - x'_j|, \quad (\text{A14})$$

where the $g_i = g(x_i) = g(x(u_i))$ (and g'_j) are precomputed in a single pass using a direct integration of $d\theta/du$, following Eq. (A12), requiring $\mathcal{O}(K)$ operations.

The quasiseparable form of the pairwise interaction potential allows us to rewrite Eq. (A14) as

$$\psi_{kk'}(J, J') = \frac{4G}{\pi^2 K^2} \sum_{j=1}^K g'_j (P_j + Q_j), \quad (\text{A15})$$

with the cumulative sums

$$P_j = \sum_{i=1}^{w_j} g_i (x'_j - x_i), \quad Q_j = \sum_{i=w_j+1}^K g_i (x_i - x'_j), \quad (\text{A16})$$

and $w_j = \text{Card}\{i \in \llbracket 1, K \rrbracket \mid x_i \leq x'_j\}$. Importantly, P_j and Q_j can both be computed in a single pass, requiring overall $\mathcal{O}(K)$ operations to estimate $\psi_{kk'}(J, J')$. In practice, we used $K = 10^3$ nodes, and an RK4 scheme to compute g_i, g'_j . We note that for $k \gg 1$, $\psi_{kk}(J, J) \propto 1/k^2$, which explains the minor role played by high order resonances, as in Fig. 6.

5. Computing the response matrix

The response matrix from Eq. (11) involves a sum over the resonances k , and an integral over the action J with a resonant denominator. This asks for a careful treatment.

Benefiting from the rapid decay of the coupling coefficients, we can safely truncate the sum over k to $|k| \leq k_{\max}$. In practice, $k_{\max} = 10$ proves highly sufficient.

To deal with the resonant integral from Eq. (11), we follow the approach from Ref. [43]:

(1) The truncated action domain $[J_0, J_L]$ [with $J_0 = J(r_a = 0)$ and $J_L = J(r_a = L)$] is remapped to $[-1, 1]$ via $y = \text{Sign}(k)[\Omega(J) - \Sigma_\Omega]/\Delta_\Omega$ with $\Sigma_\Omega = \frac{1}{2}(\Omega_0 + \Omega_L)$, $\Delta_\Omega = \frac{1}{2}(\Omega_0 - \Omega_L)$, $\Omega_0 = \Omega(J_0)$, and $\Omega_L = \Omega(J_L)$. Equation (11) then becomes

$$M_k^{pq}(\omega) = \int_{-1}^1 dy \frac{G_k^{pq}(y)}{y - \varpi_k}, \quad (\text{A17})$$

with

$$G_k^{pq}(y) = 2\pi \text{Sign}(k) \frac{dJ}{d\Omega} \frac{\partial F}{\partial J} \psi_k^{(p)*}(J) \psi_k^{(q)}(J), \quad (\text{A18a})$$

$$\varpi_k = \frac{\omega}{|k|\Delta_\Omega} - \text{Sign}(k) \frac{\Sigma_\Omega}{\Delta_\Omega}, \quad (\text{A18b})$$

where J depends implicitly on y .

(2) The numerator $G_k^{pq}(y)$ in Eq. (A18a) is projected onto Legendre polynomials via $G_k^{pq}(y) = \sum_{\ell=0}^{\ell_{\max}} a_{k\ell}^{pq} P_\ell(y)$, using a Gauss-Legendre (GL) quadrature truncated to ℓ_{\max}

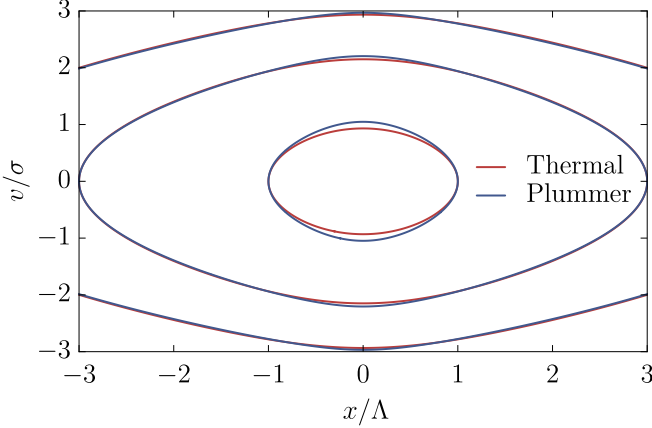


FIG. 9. Typical mean-field (closed) orbits in phase space, for apocenters $r_a/\Lambda = (1, 3, 5)$. Because the Plummer equilibrium is more peaked than the thermal one, its orbits reach a larger maximal velocity in the system's center.

(= 100 in practice). Equation (A17) then becomes $M_k^{pq}(\omega) = \sum_{\ell=0}^{\ell_{\max}} a_{k\ell}^{pq} D_{k\ell}(\omega)$ with

$$D_{k\ell}(\omega) = \int_{-1}^1 dy \frac{P_\ell(y)}{y - \omega_k}. \quad (\text{A19})$$

(3) We apply Landau's prescription [see, e.g., Sec. 5.2.4 in [2]] to compute D_{k0} and D_{k1} , while $D_{k\ell}$ for $\ell \geq 2$ are computed via direct recurrences [see Appendix D in [43]].

6. Quasistationary states

The equilibrium DFs presented in Sec. II B are obtained by Eddington inversion [see, e.g., Sec. 4.3.1 in [2]]. For a symmetric density profile, the density $\rho(r = |x|) = 2 \int_0^{+\infty} dv F(E)$, can be expressed as

$$\rho(\psi) = \sqrt{2} \int_{\psi}^{+\infty} dE \frac{F(E)}{\sqrt{E - \psi}}, \quad (\text{A20})$$

with $\psi = \psi(r)$. Following Eq. (B.72) of Ref. [2], this Abel integral equation is inverted as

$$F(E) = \frac{\sqrt{2}}{\pi} \int_E^{+\infty} d\psi \sqrt{\psi - E} \frac{d^2 \rho}{d\psi^2}. \quad (\text{A21})$$

Finally, using the relation $\psi(x) = \int dx' \rho(x') U(x, x')$, one readily finds the potential of the thermal equilibrium

$$\psi(x) = GM_{\text{tot}} \Lambda \log [2 \cosh (x/\Lambda)], \quad (\text{A22})$$

as well for the Plummer quasistationary equilibrium

$$\psi(x) = GM_{\text{tot}} \alpha \sqrt{1 + (x/\alpha)^2}. \quad (\text{A23})$$

The DF from Eq. (4) is the usual Boltzmann distribution $F(E) \propto e^{-mE/k_B T}$ of statistical mechanics with the specific energy E , and a thermodynamical temperature $k_B T = mE_0/2$. Using the virial theorem, one can relate the total energy E_{tot} to the temperature T , characteristic velocity σ , and characteristic length Λ by $E_{\text{tot}} = \frac{3}{2} N k_B T = \frac{3}{4} M_{\text{tot}} \sigma^2 = \frac{3}{4} G M_{\text{tot}}^2 \Lambda$.

Figure 9 illustrates typical mean-field orbit in the thermal and Plummer equilibria. Both display similar phase-space

diagrams, although Plummer's orbits reach larger central velocity owing to their denser core (Fig. 1).

APPENDIX B: N-BODY INTEGRATION

1. Method

The system's total Hamiltonian is

$$H_{\text{tot}} = \sum_{i=1}^N \frac{1}{2} m_i v_i^2 + \sum_{i<j} m_i m_j U(x_i, x_j), \quad (\text{B1})$$

so that the equations of motion for particle i read

$$\dot{x}_i = v_i; \quad \dot{v}_i = G(M_i^r - M_i^l), \quad (\text{B2})$$

with M_i^r (respectively, M_i^l) the total mass on the right (respectively, on the left) of particle i . Importantly, by sorting the set $\{x_i\}$, one can compute these cumulative masses in a single pass. Determining the (exact) instantaneous forces on all particles requires therefore $\mathcal{O}[N \ln(N)]$ operations.

The present 1D system can be integrated exactly using a collision-driven scheme [44]. However, this approach requires $\mathcal{O}[N^2 \ln(N)]$ operations per dynamical time, making long-time integrations of large- N systems too challenging. As such, we rather settle on using an approximate time integrator (with exact forces). Because Eq. (B1) is separable, one can use standard splitting methods [see, e.g., [45]] to devise integration schemes. The main source of error comes from the abrupt force changes every time particles cross, making it wiser to limit oneself to low-order schemes. We use the standard leapfrog scheme [see, e.g., Sec. 3.4.1 in [2]] which requires a single (costly) force evaluation per timestep, δt , and an overall $\mathcal{O}[N \ln(N) t_{\text{dyn}}/\delta t]$ operations per dynamical time.

In Fig. 10, we check the sanity of our algorithm, by illustrating the conservation of the total energy, E_{tot} , as one varies the timestep δt , the number of particles, N , and the overall number of integration timesteps, $t/\delta t$. Because the pairwise interaction, $U(x, x')$, does not have a continuous derivative, the leapfrog scheme is only first-order accurate, i.e., its error scales like $\mathcal{O}(\delta t)$ after a fixed finite-time (top panel). As one increases N , these discontinuities weaken, so that the error at finite time scales like $\mathcal{O}(1/N)$ (center panel). Finally, for the present explicit scheme, we empirically find that the error in E_{tot} grows like \sqrt{t} as a function of time (bottom panel).

To prevent the N -body realizations from drifting away, we systematically perform the operation $v_i \leftarrow v_i - \sum_{i=1}^N m_i v_i / M_{\text{tot}}$ at the simulation's onset, hence setting the system's total momentum to zero. Such a recentring slightly blurs the effective DF in velocity space (and therefore in energy) by an amount proportional to $1/\sqrt{N}$. To mitigate this effect, we always chose values of N large enough, e.g., $N = 10^5$ as in Fig. 2.

In the Landau simulations, we introduce two types of particles: (i) massive background particles that follow the smooth mean potential, and (ii) massless test particles driven by the instantaneous (noisy) potential generated by the background particles. While the background particles follow the unperturbed mean-field orbits, the orbits of test particles are slightly altered by the bare potential fluctuations in which they are embedded. The orbital diffusion undergone by these test particles corresponds to the (undressed) Landau diffusion. Such

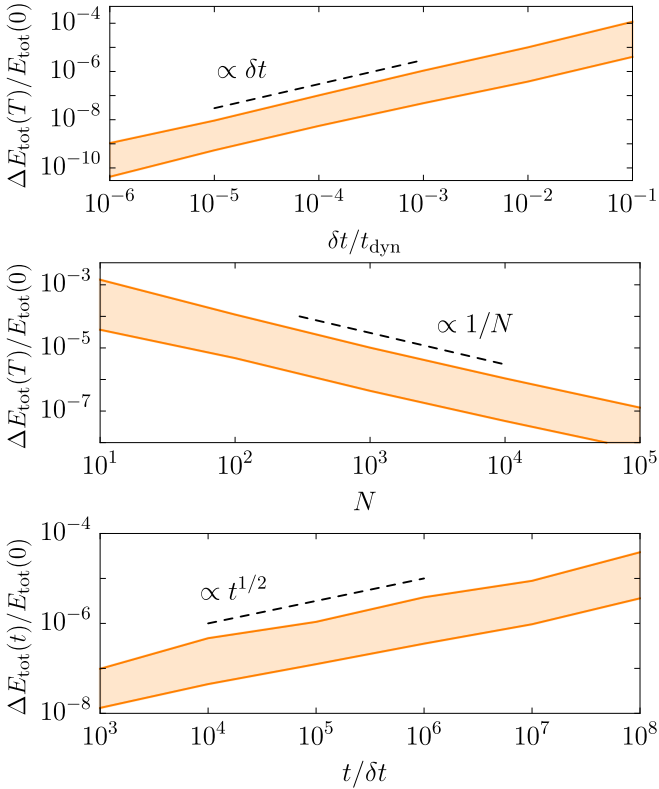


FIG. 10. Relative error in the system's total energy, E_{tot} , as a function of (i) the timestep δt (with $N = 10^4$, $T/t_{\text{dyn}} = 100$), (ii) the number of particles N (with $\delta t/t_{\text{dyn}} = 10^{-3}$, $T/t_{\text{dyn}} = 100$), (iii) the total number of integration steps $t/\delta t$ (with $N = 10^4$, $\delta t/t_{\text{dyn}} = 10^{-3}$).

simulations only keep track of the Landau diffusion. They do not mimic the Landau flux as massless test particles do not undergo any friction [46].

2. Diffusion measurements

To estimate diffusion coefficients in N -body simulations, we follow Eq. (10). First, for the sake of convenience, we measure diffusion in energy, $E = v^2/2 + \psi(x)$, computed with $\psi(x)$ the system's initial unperturbed potential. For a given realization, particles are initially binned in 25 bins of width $\delta E_{\text{bin}} = 0.1 E_0$ starting at the minimal energy $\psi(0)$. For every bin and every time dump, we compute $\langle \Delta E^2(t) \rangle = \langle [E(t) - E(t=0)]^2 \rangle$, averaged over all the particles initially in the bin and all the available realizations. In practice, the associated time series, $t \rightarrow \langle \Delta E^2(t) \rangle$ is truncated at a time T_{max} chosen so that $\langle \Delta E^2(T_{\text{max}}) \rangle \leq \delta E_{\text{bin}}^2$. This ensures that particles have not diffused so much as to explore too different energies.

Because the system's fluctuations are correlated, the series of $\langle \Delta E^2 \rangle$ are not always linear function of time, but exhibit initially a quadratic dependence w.r.t. time. This occurs during the ballistic time, T_{bal} , which, fortunately is independent of N (see Fig. 4). It is important not to perform any measurement within this early phase. A final caveat stems from the fact that at large time, the BL time series become sub-linear, a phenomenon already noted in the HMF model [see Fig. 8

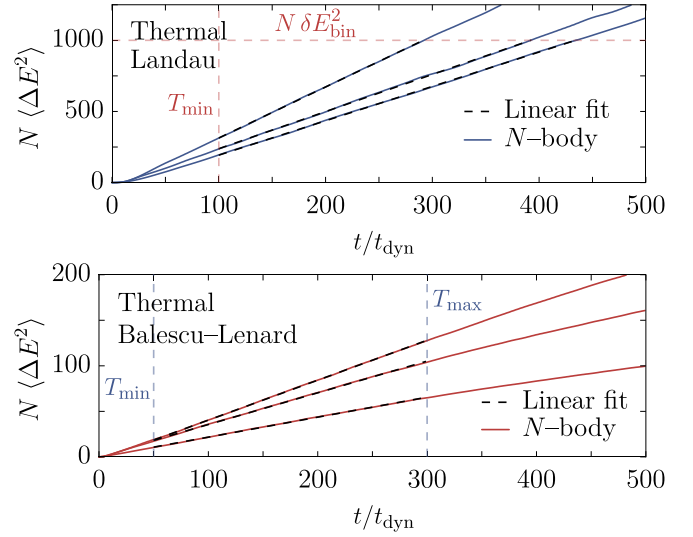


FIG. 11. Typical time series of energy dispersion averaged over a given energy bin and 1280 realizations for Landau (top panel) and BL measurements (bottom), together with the associated linear fit. Here, $\langle \Delta E^2 \rangle$ first evolves quadratically in time (ballistic regime) and then linearly (diffusive regime). For the BL experiments, the time series ultimately becomes sublinear, as already noted in the HMF model [18].

in [18]]. This is accounted for by appropriately reducing the series' maximal time, T_{max} , so as not to enter this regime.

Once the domain $T_{\text{bal}} \leq t \leq T_{\text{max}}$ determined, we rely on Eq. (10) and estimate the diffusion coefficient with a linear fit (least squares) on that timespan. This is illustrated in Fig. 11 for both Landau and BL measurements.

For the BL measurements in Fig. 2, we ran 10 independent groups of 1280 realizations with $N = 10^5$ particles, with $\delta t = 10^{-3} t_{\text{dyn}}$ up to $T = 500 t_{\text{dyn}}$, reaching a typical relative error in E_{tot} of order 10^{-6} , and dumping ΔE^2 values every t_{dyn} . As illustrated in Fig. 11, we performed the linear fit within the domain $[T_{\text{bal}}, T_{\text{max}}] = [50 t_{\text{dyn}}, 300 t_{\text{dyn}}]$. In Fig. 2, we report the mean value and standard deviation of the 10 independent batches of realizations.

For the Landau experiments, we use the exact same parameters, except that the $N = 10^5$ massive background particles follow the smooth mean potential, and we injected 2×10^4 massless test particles sampled initially according to $F(E)$. Because Landau simulations exhibit longer correlation times (see Fig. 4), we use $T_{\text{bal}} = 100 t_{\text{dyn}}$ and adjusted T_{max} for every bin so that $\langle \Delta E^2(T_{\text{max}}) \rangle \leq \delta E_{\text{bin}}^2$, as illustrated in Fig. 11.

3. Flux measurements

To estimate the diffusion flux from Eq. (8), we rely on the easy to measure cumulative density of state (DoS),

$$G(E) = \int_{-\infty}^E dE' P(E'), \quad (\text{B3})$$

with $P(E) = 2\pi F(E)/\Omega(E)$ the DoS in energy, normalized so that $\int dE P(E) = 1$. Following Eq. (8a), we naturally have $dG/dt = -2\pi \mathcal{F}(E)$. Consequently, to measure the flux, we simply count the number of particles with an (unperturbed)

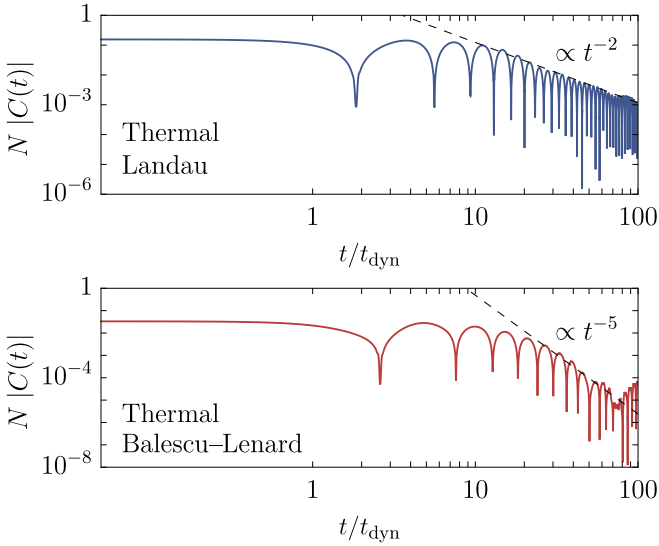


FIG. 12. Fit of the decay rate of the correlation $C(t)$ from Fig. 4 for the Landau (top) and BL cases (bottom) using 12 800 realizations.

energy smaller than a given energy threshold E , and keep track of this quantity as a function of time. Once averaged over realizations, the flux, $\mathcal{F}(E)$, is directly estimated via linear fits. These measurements are more challenging than that of the diffusion coefficients because the Plummer flux is particularly small (Fig. 3).

In practice, we ran 10 independent groups of 1280 realizations with $N = 10^4$ particles, with $\delta t = 10^{-3} t_{\text{dyn}}$ up to $T = 10^4 t_{\text{dyn}}$, reaching a typical relative error on E_{tot} of order 10^{-5} , and dumping values of interest every $10 t_{\text{dyn}}$. In Fig. 3, we report the mean value and standard deviations over these 10 independent batches.

4. Correlation measurements

As emphasized in Ref. [30], orbital diffusion is generically sourced by the time correlation of the potential fluctuations, which here stem from Poisson shot noise. The instantaneous density $\rho_d(x, t) = \sum_i m \delta_D[x - x_i(t)]$ can easily be projected onto the biorthogonal basis (Appendix A 2) to write $\rho_d(x, t) = \sum_p A_p(t) \rho^{(p)}(x)$ with

$$A_p(t) = - \sum_i m \psi^{(p)}[x_i(t)]. \quad (\text{B4})$$

We use these coefficients to probe the time evolution of the system's finite- N fluctuations. More precisely, we consider $\delta A_p(t) = A_p(t) - \langle A_p \rangle_t$, with $\langle A_p \rangle_t$ the time-average over the simulated duration. In Fig. 4, we illustrate the correlation

$$C(t) = \int_0^{T-t} \frac{d\tau}{T-t} \langle \delta A_p(\tau) \delta A_p(\tau+t) \rangle, \quad (\text{B5})$$

where $\langle \cdot \rangle$ stands for the average over realizations, for the odd basis element $\psi_{\text{odd}}^{(3)}$, following Eq. (A8). In practice, we ran 12 800 realizations of the thermal equilibrium with $N = 10^5$ particles, with $\delta t = 10^{-3} t_{\text{dyn}}$ up to $T = 10^3 t_{\text{dyn}}$, reaching a typical relative error on E_{tot} of order 10^{-6} , and dumping values of A_p every $0.05 t_{\text{dyn}}$. For the BL experiment, we also let the system “warm up” during 200 dynamical times before any measurement, so as to let the initial Poisson shot noise thermalize and get dressed by collective effects [see, e.g., Appendix F in [29]].

Decay rates are estimated through linear regressions of the local extrema in log-log scale as illustrated in Fig. 12. The ballistic time is shorter for the BL experiments, as (i) the typical amplitude of the BL correlation is lower than the Landau ones and (ii) correlations decay faster in the presence of collective effects.

-
- [1] D. Lynden-Bell, *Mon. Not. R. Astron. Soc.* **136**, 101 (1967).
[2] J. Binney and S. Tremaine, *Galactic Dynamics*, 2nd ed. (Princeton University Press, Princeton, NJ, 2008).
[3] J. Heyvaerts, *Mon. Not. R. Astron. Soc.* **407**, 355 (2010).
[4] P.-H. Chavanis, *Physica A* **391**, 3680 (2012).
[5] J.-B. Fouvry, C. Pichon, J. Magorrian, and P.-H. Chavanis, *Astron. Astrophys.* **584**, A129 (2015).
[6] J.-B. Fouvry, C. Hamilton, S. Rozier, and C. Pichon, *Mon. Not. R. Astron. Soc.* **508**, 2210 (2021).
[7] F. Hohl and J. W. Campbell, *Astron. J.* **73**, 611 (1968).
[8] J. Reidl, Charles J., and B. N. Miller, *Astrophys. J.* **332**, 619 (1988).
[9] T. N. Teles, Y. Levin, and R. Pakter, *Mon. Not. R. Astron. Soc.: Lett.* **417**, L21(2011).
[10] M. Joyce and T. Worrakitpoonpon, *J. Stat. Mech.* (2010) P10012.
[11] L. F. Souza and T. M. R. Filho, *arXiv:2007.11635* (2020).
[12] H. L. Wright, B. N. Miller, and W. E. Stein, *Astrophys. Space Sci.* **84**, 421 (1982).
[13] K. R. Yawn and B. N. Miller, *Phys. Rev. E* **56**, 2429 (1997).
[14] M. Solway, J. A. Sellwood, and R. Schönrich, *Mon. Not. R. Astron. Soc.* **422**, 1363 (2012).
[15] J. Bovy *et al.*, *Astrophys. J.* **753**, 148 (2012).
[16] Y. B. Zel'dovich, *Astron. Astrophys.* **5**, 84 (1970).
[17] P. Valageas, *Phys. Rev. E* **74**, 016606 (2006).
[18] F. P. C. Benetti and B. Marcos, *Phys. Rev. E* **95**, 022111 (2017).
[19] T. Padmanabhan, *Phys. Rep.* **188**, 285 (1990).
[20] B. N. Miller and P. Youngkins, *Phys. Rev. Lett.* **81**, 4794 (1998).
[21] P. H. Chavanis, *Int. J. Mod. Phys. B* **20**, 3113 (2006).
[22] J. Spitzer, Lyman, *Astrophys. J.* **95**, 329 (1942).
[23] G. L. Camm, *Mon. Not. R. Astron. Soc.* **110**, 305 (1950).
[24] G. B. Rybicki, *Astrophys. Space Sci.* **14**, 56 (1971).
[25] A. S. Eddington, *Mon. Not. R. Astron. Soc.* **76**, 572 (1916).
[26] M. Hénon, *Astron. Astrophys.* **24**, 229 (1973).
[27] G. P. Horedt, *Polytropes* (Kluwer Academic Publishers, Amsterdam, 2004).
[28] P.-H. Chavanis, *Astron. Astrophys.* **556**, A93 (2013).
[29] J.-B. Fouvry and B. Bar-Or, *Mon. Not. R. Astron. Soc.* **481**, 4566 (2018).
[30] J. Binney and C. Lacey, *Mon. Not. R. Astron. Soc.* **230**, 597 (1988).
[31] J.-B. Fouvry, P.-H. Chavanis, and C. Pichon, *Phys. Rev. E* **102**, 052110 (2020).

- [32] J. Magorrian, *Mon. Not. R. Astron. Soc.* **507**, 4840 (2021).
- [33] M. D. Weinberg, *Mon. Not. R. Astron. Soc.* **239**, 549 (1989).
- [34] M. D. Weinberg, *Astrophys. J.* **421**, 481 (1994).
- [35] M. D. Weinberg, *Mon. Not. R. Astron. Soc.* **328**, 321 (2001).
- [36] J.-B. Fouvry, C. Pichon, P.-H. Chavanis, and L. Monk, *Mon. Not. R. Astron. Soc.* **471**, 2642 (2017).
- [37] <https://www.secular-evolution.org/>.
- [38] <https://github.com/MathieuRoule/odiBLE>.
- [39] M. Hénon, *Astrophys. Space Sci.* **13**, 284 (1971).
- [40] A. J. Kalnajs, *Astrophys. J.* **205**, 745 (1976).
- [41] W. Press *et al.*, *Numerical Recipes*, 3rd ed. (Cambridge University Press, Cambridge, UK, 2007).
- [42] S. Rozier *et al.*, *Mon. Not. R. Astron. Soc.* **487**, 711 (2019).
- [43] J.-B. Fouvry and S. Prunet, *Mon. Not. R. Astron. Soc.* **509**, 2443 (2022).
- [44] A. Noullez, D. Fanelli, and E. Aurell, *J. Comput. Phys.* **186**, 697 (2003).
- [45] E. Hairer, C. Lubich, and G. Wanner, *Geometric Numerical Integration*, 2nd ed. (Springer, Berlin, 2006).
- [46] R. W. Nelson and S. Tremaine, *Mon. Not. R. Astron. Soc.* **306**, 1 (1999).